J Neurophysiol 113: 3242–3255, 2015.
First published March 5, 2015; doi:10.1152/jn.00624.2014.

Microcircuitry of agranular frontal cortex: contrasting laminar connectivity between occipital and frontal areas

Taihei Ninomiya, Kacie Dougherty, David C. Godlove, Jeffrey D. Schall, and Alexander Maier
Department of Psychology, Vanderbilt Vision Research Center, Center for Integrative and Cognitive Neuroscience, and Vanderbilt Brain Institute, Vanderbilt University, Nashville, Tennessee

Submitted 19 August 2014; accepted in final form 3 March 2015

Ninomiya T, Dougherty K, Godlove DC, Schall JD, Maier A. Microcircuitry of agranular frontal cortex: contrasting laminar connectivity between occipital and frontal areas. *J Neurophysiol* 113: 3242–3255, 2015. First published March 5, 2015; doi:10.1152/jn.00624.2014.—Neocortex is striking in its laminar architecture. Tracer studies have uncovered anatomical connectivity among laminae, but the functional connectivity between laminar compartments is still largely unknown. Such functional connectivity can be discerned through spontaneous neural correlations during rest. Previous work demonstrated a robust pattern of mesoscopic resting-state connectivity in macaque primary visual cortex (V1) through interlaminar cross-frequency coupling. Here we investigated whether this pattern generalizes to other cortical areas by comparing resting-state laminar connectivity between V1 and the supplementary eye field (SEF), a frontal area lacking a granular layer 4 (L4). Local field potentials (LFPs) were recorded with linear microelectrode arrays from all laminae of granular V1 and agranular SEF while monkeys rested in darkness. We found substantial differences in the relationship between the amplitude of gamma-band (>30 Hz) LFP and the phase of alpha-band (7–14 Hz) LFP between these areas. In V1, gamma amplitudes in L2/3 and L5 were coupled with alpha-band LFP phase in L5, as previously described. In contrast, in SEF phase-amplitude coupling was prominent within L3 and much weaker across layers. These results suggest that laminar interactions in agranular SEF are unlike those in granular V1. Thus the intrinsic functional connectivity of the cortical microcircuit does not seem to generalize across cortical areas.

cross-frequency coupling; phase-amplitude coupling; canonical microcircuit; cortical column; spontaneous activity; ongoing activity

SINCE BRODMANN'S INFLUENTIAL PAPER (Brodmann 1909), many neuroanatomists have reported heterogeneity in cytoarchitecture across the primate neocortex. A vivid example of regional diversity is provided by comparing the granular primary visual area (V1) in the occipital lobe and the agranular supplementary eye field (SEF) in the frontal lobe. V1 has a thick granular layer 4 (L4) where dense thalamic terminals are concentrated, whereas SEF lacks a granular L4 (Barbas and Pandya 1987; Brodmann 1909; Shipp 2005; Walker 1940).

The anatomical distinctions between granular visual cortex and agranular SEF suggest that neuronal interactions within and between laminae may differ between these two regions. To characterize laminar microcircuitry within SEF, Godlove et al. (2014) recently described the visually evoked current source density (CSD) pattern of that area. They reported visually evoked current sinks in middle layers followed by sinks in superficial and deep layers. This sequence is broadly consistent with the laminar response pattern observed in early visual areas. However, unlike visual cortex, SEF exhibited two separate, early current sinks in its middle layers. While the spatiotemporal results from the visually evoked CSD provide insight into the sequence of activation among layers, it cannot differentiate neural activity caused by interareal projections from activity caused by local microcircuitry.

Spaak et al. (2012) recently addressed this question of local connectivity in V1 by characterizing the correlational pattern of resting-state local field potentials (LFPs) in separate layers. Specifically, gamma-band (30–200 Hz) LFP amplitude ("power") in supragranular layers was modulated with the phase of an infragranular alpha-band rhythm (7–14 Hz). This relationship is known as phase-amplitude coupling (reviewed by Canolty and Knight 2010; Jensen and Colgin 2007). Besides revealing interactions across cortical areas, it can also uncover interlaminar connections of ongoing neural activity.

Here we test the general hypothesis that a common, canonical microcircuit is replicated throughout the mammalian neocortex. This conjecture was tested by quantitatively comparing the phase-amplitude relationship of frequency components in resting-state LFPs within and across agranular SEF layers with that within and across granular V1 layers. Our data replicated a previous finding of lamina-specific phase-amplitude coupling in V1 during rest and demonstrated that this coupling occurs in SEF but reveals a fundamentally different laminar pattern compared with V1.

METHODS

Some of the methods used in this study have been described in detail elsewhere, including surgical preparation, experimental conditions, data collection, depth alignment, and electrode angle estimation (Godlove et al. 2014; Maier et al. 2010).

Surgical preparation. Four monkeys were used in this study. Two monkeys were used to collect data from area V1 (*monkeys V1-b* and *V1-h*, *Macaca radiata*; male 7.0 kg, female 7.2 kg), while two different monkeys were used to collect data from SEF (*monkey SEF-e*, *M. radiata* male 8.8 kg; *monkey SEF-x*, *M. mulatta* female 6.0 kg). All procedures were compliant with regulations set by the US Department of Agriculture (USDA), the Office of Laboratory Animal Welfare (OWLA), and the Association for Assessment and Accreditation of Laboratory Animal Care (AAALAC) and approved by the Vanderbilt University Institutional Animal Care and Use Committee (IACUC).

Data collection. Although recordings in V1 and in SEF were conducted in different laboratories, the techniques were largely similar. During each experimental session, monkeys sat in a custom-made primate chair with their head restrained. The chair was positioned 73 cm in front of a 27-in. TFT monitor (Asus VG278H) for the V1 recordings and 45 cm in front of a 21-in. CRT monitor (Dell P1130) for the SEF recordings.

Address for reprint requests and other correspondence: A. Maier, Dept. of Psychology, PMB 407817, 2301 Vanderbilt Place, Vanderbilt Univ., Nashville, TN 37240-7817 (e-mail: alex.maier@vanderbilt.edu).

Data were collected with a 24-channel linear microelectrode array (Plexon U-Probe, Plexon, Dallas, TX), with an interelectrode spacing of 100 μm (V1 recordings) or 150 μm (SEF recordings). The range of impedance measured for all channels was 0.3–0.5 MΩ at 1 kHz. After inserting the linear microelectrode array into the target chamber at the desired depth, we waited 1–4 h until the recorded data indicated that the electrode had reached a stable position in cortex. After the electrode had stabilized, we recorded 7–60 min of resting-state LFP in near-total darkness with the monitor powered off. Extracellular voltages were measured over time in reference to the electrode shaft. For V1 recordings, the data were amplified and filtered in the range of 0.3 Hz–7.5 kHz, digitized at 30 kHz, and stored with the Blackrock Microsystems Cerebus system (Salt Lake City, UT). V1 LFP was extracted off-line by filtering the broadband data between 0.5 Hz and 500 Hz and decimating by a factor of 30, resulting in a sampling rate of 1 kHz. For SEF recordings, all data were streamed with the Plexon MAP system (Plexon). SEF LFP data were computed by band-pass filtering between 0.2 and 300 Hz and amplifying with a gain of 1,000, followed by digitizing at 1 kHz.

Experimental conditions. The main focus of this study is on data collected during the resting state. However, each day we also presented full-screen visual flashes in order to assess the depth of the electrode in cortex (see *Laminar electrode placement*). For V1, a flashing white light stimulus was produced with MonkeyLogic 1.2 (Asaad and Eskandar 2008) in MATLAB 2011b (32 bit) running on a PC with Windows 7 (64 bit) using an NVIDIA GeForce GTX 680 graphics board. The stimulus filled the entire screen (45° × 27°). In this passive viewing paradigm, the animal was presented with periodic 50-ms flashes of white light (luminance of 74.7 cd/m^2 in CIE color space), each followed by a 1-s black blank (0.470 cd/m^2) screen for a period of 20 min. For SEF sessions, when the monkey's gaze fell within 11° of the center of the CRT monitor a white square (34.8 cd/m^2, 14.3 ms at 70 Hz) was presented for a single frame (14.3 ms) at the central area of the CRT monitor (corresponding to the central 40° × 36° of the visual field), followed by 500 ms of a blank black screen (0.1 cd/m^2) for as long as the monkey's gaze remained in this central window. The stimulus presentation was provided in blocks of 100–200 presentations. Flash presentation and eye position monitoring were performed by dedicated computers (TEMPO, Reflective Computing, Olympia, WA; EyeLink, SR Research, Mississauga, ON, Canada). The timing of visual light flashes was measured by a photodiode positioned against the monitor.

Laminar electrode placement. Accurate laminar placement of the electrode channels was required for these experiments. This was achieved through multiple steps, checks, and tests (Fig. 1).

1) The linear microelectrode arrays were inserted slowly. Upon penetration of the dura mater, the depth of the electrode array in cortex (usually just a few hundred micrometers) was discerned by contrasting the 1/f$^\alpha$ (pink) noise profile of the neural LFP on array channels in neuropil from the Gaussian noise profile on channels outside of the brain (Fig. 1*E*). The array of channels was never fully advanced into the cortex in order to identify the depth of cortical entry. If a guide tube was used to fortify the electrode during penetration, it was retracted after the array entered the brain to ensure that no channels were occluded. Note that no penetration through the dura mater was made with a guide tube.

2) The distinction between channels inside and outside the neocortex was validated by the presence of spontaneous and visually evoked single-unit and multiunit spiking activity.

3) Converging evidence for array depth was obtained from the laminar profile of LFP gamma power (40–80 Hz), which is quantifiably attenuated on channels outside the cortex. Gamma power is typically increased in middle layers and decreased in lower layers in both V1 (Maier et al. 2010; Smith et al. 2013; Xing et al. 2012) and SEF (Godlove et al. 2014).

4) Further converging evidence for array depth in V1 was obtained from a clear separation of LFP coherence between L4C and L5 (Maier et al. 2010).

5) Further converging evidence for array depth in SEF was obtained from the laminar profile of spike width, corresponding to the histological distribution of pyramidal cells and interneurons (Godlove et al. 2014).

6) Further converging evidence for array depth was provided by the distinctive laminar profile of the visually evoked CSD in V1 (Hansen et al. 2012; Kajikawa and Schroeder 2011; Schroeder et al. 1998; Self et al. 2013) and in SEF (Godlove et al. 2014) (Fig. 1*F*). This approach is detailed in the next section.

7) Further converging evidence for proximity to the pial surface was marked by a commonly observed electrocardiogram signal (Godlove et al. 2014) (Fig. 1*F*).

8) These neurophysiological criteria were supplemented with several imaging techniques to verify both cortical penetration depth and orthogonality of the electrode to the cortical surface with high-resolution MRI (Maier et al. 2008) and a combination of CT scans and MRI (Godlove et al. 2014) (Fig. 1, *A–D*).

Previous work has established that similar criteria for matching penetration depth and distinction of laminar compartments correspond to the position of deliberately placed electrolytic lesions when verified in histological sections (Schroeder et al. 1998).

Intersession alignment of laminar data. Each recording session resulted in time-varying voltage from each of the 24 electrode channels. To average data aligned for cortical depth of the array across sessions, we employed CSD analysis of visual responses to brief flashes of light (Maier et al. 2010; Fig. 1*F*). After constructing event-related LFPs, triggering to the onset of each flash, and averaging across samples, we calculated the second spatial derivative defined by a three-point formula:

$$\mathrm{CSD} = -\frac{X(t, c-z) - 2X(\mathrm{t}, \mathrm{c}) + X(t, c+z)}{z^2}$$

where X is the extracellular voltage recorded in microvolts at time t from an electrode channel at position c and z is the electrode interchannel distance (100 μm for V1 recordings and 150 μm for SEF recordings) (Nicholson and Freeman 1975). To convert this measure into units of current per unit volume, we multiplied the result by an estimate of the conductivity of cortex, 0.4 S/m (Logothetis et al. 2007).

The location of granular L4C in V1 is uniquely characterized by an early current sink, reflecting the excitatory postsynaptic potentials produced by geniculate activation (Mitzdorf and Singer 1979). We identified the channel positioned at the bottom of this initial current sink, typically located 0.8–1.3 μm below the dura, and aligned array depths across sessions on this reference point (Maier et al. 2010). Data from SEF were aligned with an automated approach that finds the optimum depth estimates by minimizing the summed differences between every CSD profile in the data set (Godlove et al. 2014).

Data analysis. Data analyses were performed in MATLAB (R2013a, MathWorks, Natick, MA) with custom-written scripts and with the FieldTrip toolbox (Oostenveld et al. 2011). Analyses in this report parallel precisely and extend those described in Spaak et al. (2012).

Time-frequency representations (TFRs) and a modulation index (MI) were computed with bipolar derivations of LFPs obtained by rereferencing each electrode channel (excluding the most superficial) to one located 200 μm (V1) or 150 μm (SEF) in the superficial direction. This procedure attenuates the effects of electric volume conduction, resulting in more spatially precise evaluation of the local coupling within and between cortical layers.

The data from V1 were further subselected with the bipolar LFPs at electrode channels positioned +900, +300, −200, and −500 μm relative to the bottom of the initial L4 sink, thus providing 1,510, 1,521, 1,441, and 897 high alpha segments, respectively, during 432 min of recordings. In SEF, we chose the four electrode channels

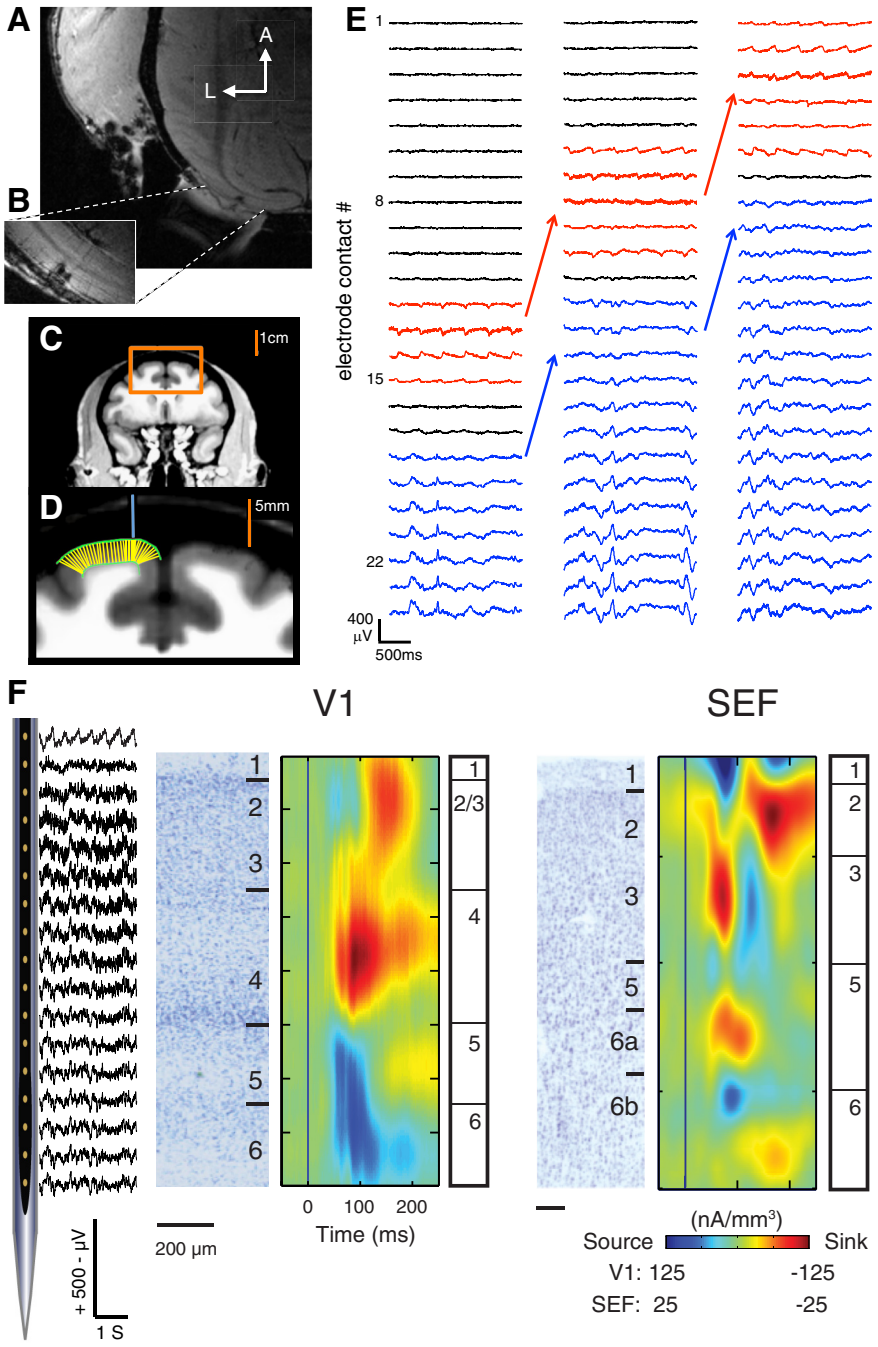

Fig. 1. Laminar electrode placement. *A*: anatomical MR image of primary visual cortex (V1) after electrode removal, revealing penetration tracks. The implanted recording chamber can be seen extending caudally. *B*: magnified MRI scan of V1, showing 2 adjacent, parallel electrode penetration tracks. Note that the MR image does not directly show the cortical lesion but instead the larger magnetic field distortion (susceptibility artifact) caused by the cerebrospinal fluid that has entered the track. *C*: anatomical MR image of supplementary eye field (SEF). *D*: magnified image of region outlined in *C*. A CT scan of the linear microelectrode array inside the recording chamber (blue line) was coregistered with the MRI. After the boundaries between gray/white matter and gray matter/skull were manually drawn (green lines), an automated algorithm determined the perpendicular lines along the boundaries (thin yellow lines). Note the perpendicularity of the electrode to the cortical surface. *E*: recordings of physiological signals during electrode placement. The electrode was advanced ~500 μm between successive recordings. Note the advancement of the electrocardiogram (red lines) and 1/f neural data (blue lines). *F*: schematic illustration of electrode configuration. Local field potentials (LFPs) were recorded simultaneously across layers of V1 or SEF with the linear multielectrode array. The location of each electrode channel was estimated by the visually evoked current source density (CSD) for each session, which was also used to align the data in depth across sessions. Grand average visually evoked CSDs are shown beside Nissl sections of V1 and SEF.

exhibiting the highest-magnitude visually evoked current sinks (+450, 0, −750, and −1350 μm relative to the location of the highest-magnitude visually evoked current sink in L3), which provided 1,519, 1,541, 1,678, and 1,392 high alpha segments, respectively, in 621 min of recordings.

We extracted periods of high alpha-band power in the bipolar LFPs for each session. Specifically, bipolar LFPs were band-pass filtered (2-pass least-square finite impulse response filter with an order of 426 over 7–14 Hz) and then Hilbert-transformed to acquire the alpha-band amplitude envelope. Each high alpha segment had an amplitude above the 30th percentile of the alpha amplitude distribution within the session for a minimum time of 800 ms.

Alpha-aligned time-frequency representations. TFRs were obtained by aligning time-varying power spectra of the LFP (20–300 Hz) to alpha-band LFP peaks recorded from a single reference channel (Fig. 2*A*). More specifically, alpha peaks in the LFP were defined by identifying zero crossings in the second temporal derivative of the band-limited alpha (7–14 Hz) reference signal. To obtain each TFR, the spectral power of the bipolar LFP segments around alpha peaks was computed with a sliding time window and a single Hanning taper. Power in each frequency band was computed in 1-Hz steps from 20 to 300 Hz, with a varying window length set to 7 cycles of the frequency of interest (e.g., the window length for 20 Hz was 350 ms, and the window length for 300 Hz was 23.33 ms). These alpha-aligned TFRs were averaged and normalized relative to the average power per frequency within each channel.

To compute statistical significance, randomly shuffled TFRs were obtained by the procedure outlined above but with pairing of the LFP for phase extraction from one session with the amplitude from a different session recorded in the same area. Results were

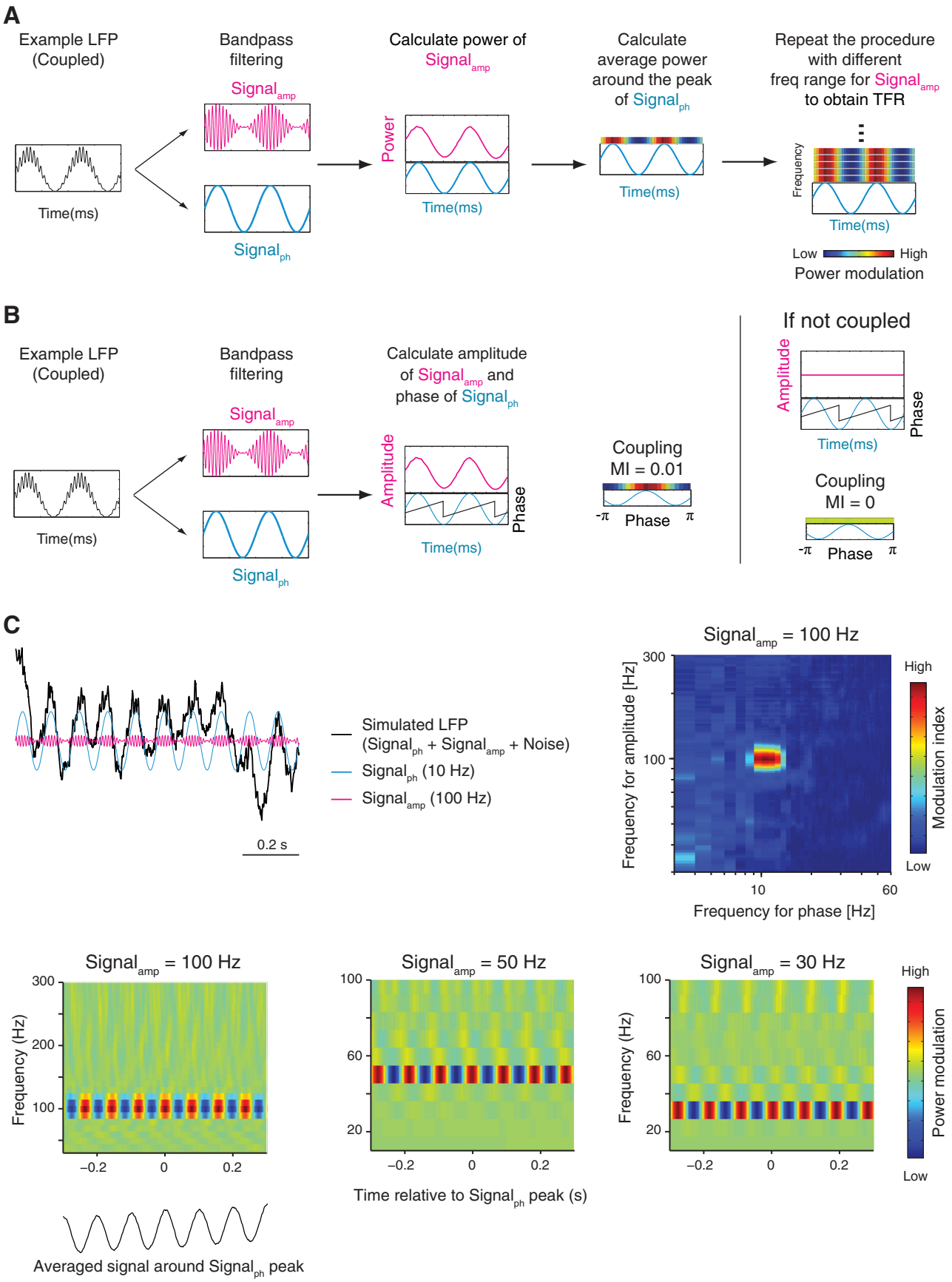
A
Example LFP (Coupled)
Bandpass filtering
Calculate power of Signal_amp
Calculate average power around the peak of Signal_ph
Repeat the procedure with different freq range for Signal_amp to obtain TFR
Signal_amp
Signal_ph
Time(ms)
Power
Frequency
Low
High
Power modulation
B
Example LFP (Coupled)
Bandpass filtering
Calculate amplitude of Signal_amp and phase of Signal_ph
Amplitude
Phase
Coupling MI = 0.01
-π
π
If not coupled
Coupling MI = 0
C
Simulated LFP (Signal_ph + Signal_amp + Noise)
Signal_ph (10 Hz)
Signal_amp (100 Hz)
0.2 s
Signal_amp = 100 Hz
Frequency for amplitude [Hz]
Frequency for phase [Hz]
Modulation index
Signal_amp = 50 Hz
Signal_amp = 30 Hz
Frequency (Hz)
Time relative to Signal_ph peak (s)
Power modulation
Averaged signal around Signal_ph peak

converted into *t*-scores, by comparing the alpha-aligned TFRs to the shuffled TFRs, for cluster-based statistical testing (Maris and Oostenveld 2007). We selected four representative channels from different laminar compartments to assess the relationship between the alpha-band peaks and LFP power within and across the cortical layers. We computed TFRs for the four channels relative to each alpha reference electrode channel, resulting in 16 TFR combinations for both SEF and V1.

Modulation index. The strength of phase-amplitude coupling was quantified with the MI proposed by Tort et al. (2010) (Fig. 2*B*). First, the bipolar LFP during periods of high alpha-band power was band-pass filtered into 2-Hz-wide bands centered on the frequency of interest, f_{phase}, for all electrode channels. Then the instantaneous phase of a given frequency was estimated by extracting the angle of the Hilbert-transformed bipolar band-limited LFP. To analyze the amplitude of the LFP, bipolar LFPs from all electrode channels during the high alpha periods (see *Data analysis*) were band-pass filtered into 10-Hz-wide bands, centered on f_{amp}. The Hilbert transform was applied to these band-limited segments, and the instantaneous amplitude was extracted by taking the absolute value of the output of the Hilbert transform. The MI was computed for all pairs of frequency bands, f_{phase} and f_{amp}, in 1-Hz steps from 3 to 60 Hz and from 30 to 300 Hz, respectively. A matrix of MI values across frequencies for phase versus amplitude was obtained with this procedure. The statistical significance of MI values was assessed with a random permutation test (using 1,000 shuffles) (Spaak et al. 2012). Significant MI values were averaged over the alpha (7–14 Hz) and gamma (30–200 Hz) bands to obtain a single MI value for each pair of bipolar LFPs. This yielded a matrix of mean MI values with each element corresponding to a specific combination of cortical depth for alpha phase and cortical depth for gamma amplitude. The MI matrix of the intersession averages was cubic spline interpolated 10-fold across space. The MI matrices were trimmed after averaging so that each data point shown reflects the average over the number of sessions indicated. Each element of the MI matrix was converted to a *t*-score using the shuffled MI matrices described above to perform cluster-based statistical testing (Maris and Oostenveld 2007).

Validation of TFR and MI analyses. The validity of the TFR and MI analyses was evaluated through analyses of a simulated signal. The simulated signal had three components: $Signal_{ph}$ (10-Hz sine wave), $Signal_{amp}$ (100-Hz sine wave with its amplitude coupled with $Signal_{ph}$), and $1/f^{\alpha}$ (pink) noise, with their relative amplitudes set to 5, 1, and 10^5, respectively (Fig. 2*C*). The TFR computed on the simulated signal showed power around 100 Hz modulating with the phase of $Signal_{ph}$, verifying the phase-amplitude coupling in the simulated signal (Fig. 2*C*). Similarly, the MI analysis applied to the simulated signal produced the highest values between a phase of ~10 Hz and an amplitude of 100 Hz (Fig. 2*C*).

Considerable smearing might occur in the lower frequency range of the TFRs because the length of the sliding time window is short, e.g., estimation of power at 30 Hz is based on ~2 cycles of alpha. To clarify whether such an artifact is critical, the TFR analysis was performed with $Signal_{amp}$ at low frequencies (30 Hz and 50 Hz; Fig. 2*D*). Clear modulation of power was confined around the frequency of $Signal_{amp}$, suggesting that smearing is not critical even when the TFR analysis is applied to the low frequency range.

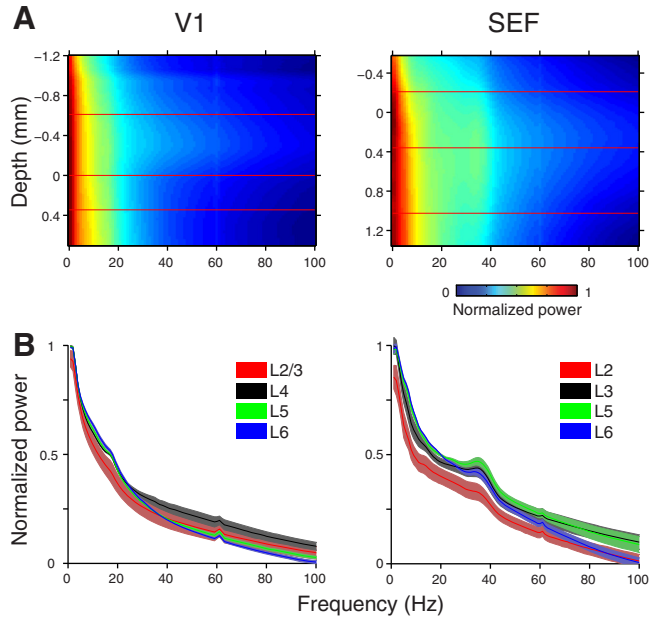

Fig. 3. Laminar distributions of LFP power in V1 and SEF. *A*: average LFP power as a function of frequency across sessions in V1 ($n = 15$) and SEF ($n = 16$). Red lines mark estimated layer borders. Note the locally increased gamma power in granular V1 compared with the more homogeneous laminar distribution of LFP power in SEF. *B*: power spectral density of LFP power for main laminar compartments (shaded regions indicate ±SE). Note the overall difference in LFP power between areas as well as the pronounced laminar segregation in SEF. The slight power peak at 60 Hz is due to a line noise artifact.

Alpha-aligned current source density analysis. For the alpha-aligned CSD analysis, alpha peaks in the unipolar LFP were detected as described above. LFP segments in a 400-ms window centered on alpha peaks were averaged for each channel. The CSD was calculated through the discrete second spatial derivative as described above. The average CSD around alpha peaks was cubic spline interpolated 10-fold across the spatial dimension. This analysis was performed on the electrode channels described in *Alpha-aligned time-frequency representations*. The statistical significance of this CSD was assessed with the procedure applied for alpha-aligned TFRs.

RESULTS

We collected laminar LFPs in V1 for 432 min (226 min over 11 sessions for *monkey V1-b*; 206 min over 12 sessions for *monkey V1-h*) and in SEF for 621 min (339 min over 7 sessions for *monkey SEF-e*; 282 min over 9 sessions for *monkey SEF-x*).

Fig. 2. *A*: schematic derivation of time-frequency representation (TFR). Example LFP segment is band-pass filtered into 2 frequency ranges of interest for amplitude ($Signal_{amp}$, red; 20–300 Hz) and for phase ($Signal_{ph}$, blue; 7–14 Hz). The spectral power of $Signal_{amp}$ is calculated with a sliding time window and triggered at every peak of $Signal_{ph}$ to obtain averaged power of $Signal_{amp}$ around the peak of $Signal_{ph}$. This procedure is repeated for each $Signal_{amp}$ frequency in 1-Hz steps from 20 to 300 Hz to obtain the full TFR. *B*: schematic derivation of the modulation index (MI). The first filtering steps are the same as for the TFR. Next, the instantaneous amplitude of $Signal_{amp}$ and the instantaneous phase of $Signal_{ph}$ are calculated with the Hilbert transform. The amplitude of $Signal_{amp}$ is binned according to the phase of $Signal_{ph}$. The MI is calculated with the algorithm proposed by Tort et al. (2010). The MI equals 0 when the amplitude is distributed uniformly across the phase cycle (*right*). *C*: application of TFR and MI analyses to simulated LFP. *Top left*: simulated LFP is the sum of 3 spectral components: $Signal_{ph}$ (10-Hz sine wave), $Signal_{amp}$ (100-Hz sine wave with amplitude coupled with $Signal_{ph}$), and $1/f^{\alpha}$ (pink) noise. *Top right*: MI matrix of simulated LFP. The procedure shown in *B* was repeated for $Signal_{ph}$ frequencies ranging from 3 to 60 Hz and $Signal_{amp}$ frequencies ranging from 30 to 300 Hz. High MI values occurred around a phase frequency of 10 Hz and amplitude frequency of 100 Hz. *Bottom*: TFRs of simulated LFP with different frequencies for $Signal_{amp}$ (100 Hz, 50 Hz, and 30 Hz from *left* to *right*, respectively). Clear modulation of power occurs around each frequency of $Signal_{amp}$ synchronized with the peaks and troughs in $Signal_{ph}$ (*bottom left*). Note that the range of the *y*-axes for the *right* 2 TFRs is different from that for the *left* TFR to reveal the entire shape of the modulation. No pronounced smearing can be seen in any TFR.

Power spectral density differences. We computed the power spectral density (PSD) of the LFP using the fast Fourier transform for each of the main laminar compartments of the two areas (Fig. 3). As reported previously for V1 (Maier et al. 2010), gamma (>40 Hz) LFP power was higher in L2/3 and L4 than in L5 and L6. In contrast, low-frequency (<10 Hz) LFP power was higher in deeper than in superficial layers. SEF exhibited a different pattern, with gamma LFP power being highest in L3 and also in L5. In summary, the distribution of power differed among laminae within each region, and the laminar pattern of LFP power was qualitatively different between the two areas.

The pattern of the laminar PSDs provided another measure to validate laminar depth alignment across sessions (Fig. 4). Data across sessions, each with the array positioned at a different depth, were aligned to minimize the difference in the laminar profile of power in the 40–80 Hz range for both V1 and SEF. Then the grand average visually evoked CSD was calculated. The CSD calculated from this alignment procedure (Fig. 4*C*) was very similar to the CSD calculated from the other alignment procedure (Fig. 1*F*). This similarity provides additional converging support for the accuracy of the intersession alignment applied in this study.

Phase-amplitude coupling differences. We next compared interlaminar interactions of LFP frequency components in both areas with cross-frequency analyses (Canolty et al. 2006; Jensen and Colgin 2007; Spaak et al. 2012). We first describe results showing that V1 and SEF differ in their respective spectral patterns of interlaminar alpha-gamma coupling. We then extend this finding by describing the laminar pattern of phase-amplitude coupling across a wider range of frequencies. Finally, we compare the laminar patterns of the alpha-related current sinks and sources in V1 and SEF.

To confirm the reliability of our data and the validity of our analytic approach, we started by evaluating whether our V1 data showed a similar laminar profile of alpha-gamma coupling, as reported in a previous study (Spaak et al. 2012). After identifying amplitude peaks in alpha-band (20–300 Hz) LFPs from L5, we computed phase-locked TFRs for LFPs recorded from L2/3, L4, L5, and L6. The result can be seen in Fig. 5. TFR colors indicate the relative amount of alpha-locked power modulation as a function of frequency, while the contours indicate significant modulations of gamma power based on a random permutation test (see METHODS for details). In line with Spaak et al. (2012), we found that gamma power in superficial layers (Fig. 5*A*) as well as in infragranular L5 (Fig. 5*C*) was significantly coupled to the phase of alpha-band LFPs in L5. Coupling was also observed between gamma power in L4 and L6 and alpha phase in L5, albeit with reduced prominence.

Performing the same analysis on the data from SEF, we made several new observations. First, the overall power modulation in SEF was not as strong as that in V1 (maximum SEF power modulation around L5 alpha phase was 3% vs. 15% around L5 alpha phase with L2/3 high gamma amplitude in V1). Second, unlike in V1, in L3 of SEF only gamma above ~150 Hz coupled with L5 alpha phase (Fig. 5*F*). Third, in further contrast to V1, gamma power in SEF L2 and L5 was only inconsistently coupled with L5 alpha phase (Fig. 5, *E* and *G*). These results are summarized in Fig. 5*I*, which shows alpha-coupled gamma amplitude for each laminar compart-

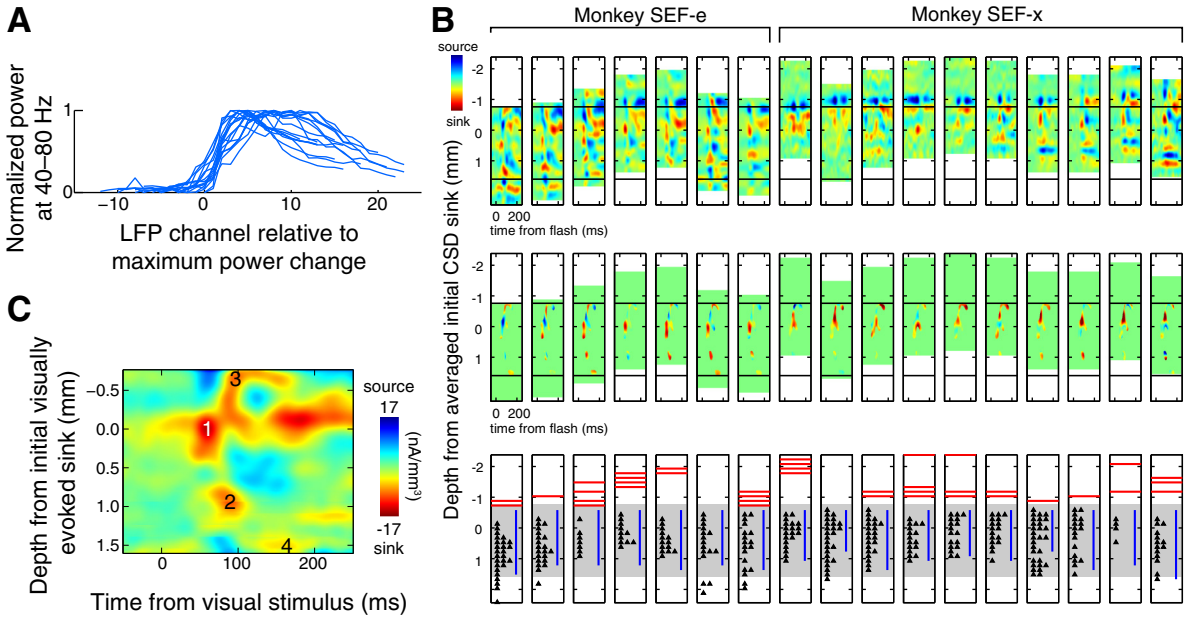

Fig. 4. Linear multielectrode array depth alignment across sessions based on LFP frequency content. *A*: normalized SEF LFP power between 40 and 80 Hz across the multielectrode array for each recording session. Each blue line represents normalized gamma power from superficial to deep electrode channels (plotted *left* to *right*) from an individual session. Gamma LFP power was generally highest in superficial layers, with a gradual decrease in deep layers. Electrode channel numbers were reassigned relative to the channel at which the maximum change in power occurred (designated *channel 0*). The invariance of this transition in power across sessions is clear. *B*: depth alignment across monkeys and sessions. *Top*: visually evoked CSD. *Middle*: visually evoked CSDs masked for significance to show laminar locations of visually evoked sinks. *Bottom*: schematic representing each day's laminar position of the electrocardiogram signal (red), cortical depths at which 40–80 Hz LFP power exceeded the average 40–80 Hz power across all electrode channels (blue), and well-isolated single units (black triangles). Horizontal black bars and gray shading indicate the estimated location of gray matter. *C*: grand average visually evoked CSD after gamma-based depth alignment. Note the presence of initial current sinks in middle (*1*) and deep (*2*) layers followed by superficial (*3*) and deep (*4*) sinks. The similarity between this intersession average and that obtained after CSD-based alignment (Fig. 1*F*) demonstrates the reliability of assigning data to particular layers in SEF.

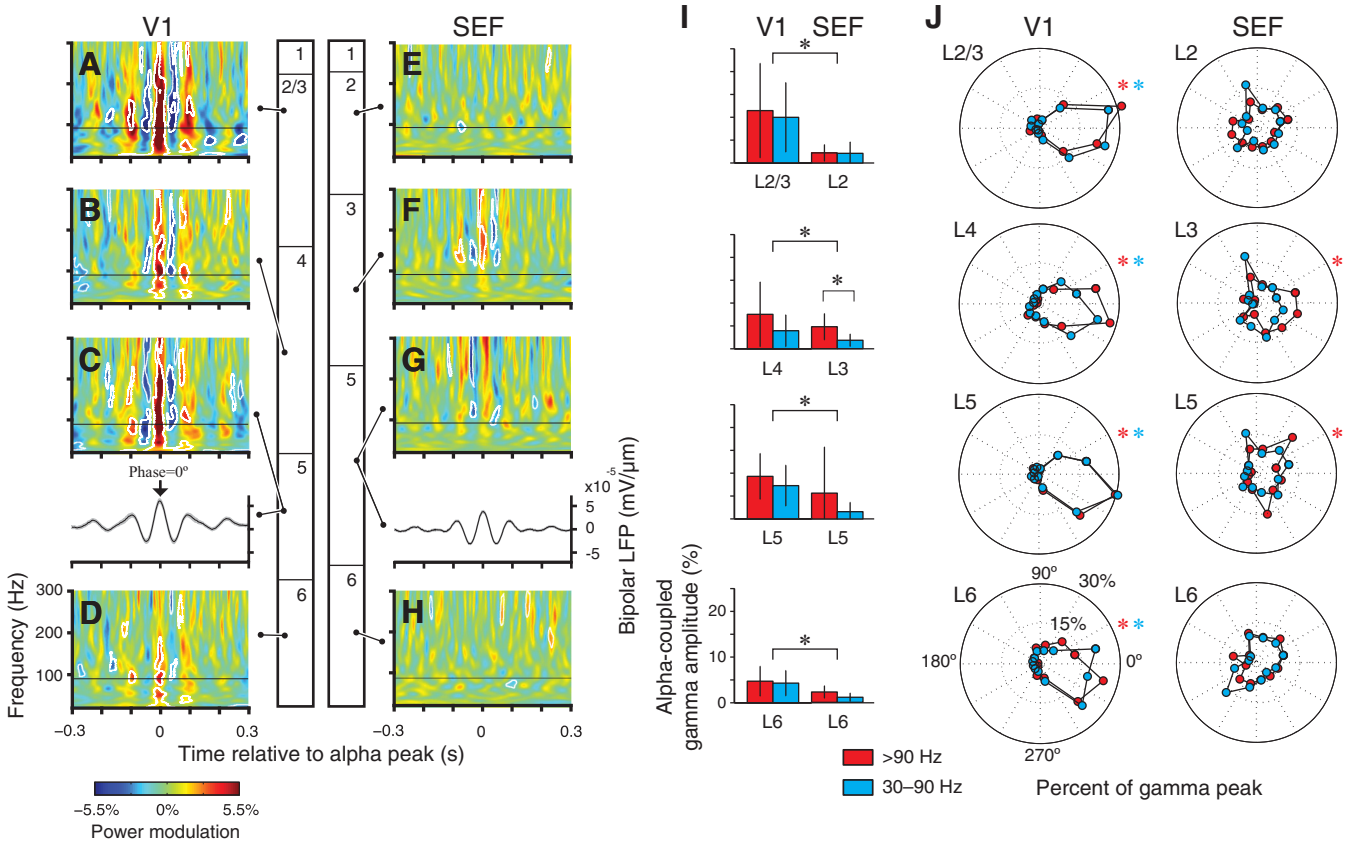

Fig. 5. Statistical quantification of phase-amplitude coupling between L5 alpha and gamma across laminar compartments in V1 and SEF. *A–D*: TFRs for increasing cortical depth (*top* to *bottom*) for area V1. Cortical lamination diagram on *right* provides a key for the respective laminar compartment compartments. Each TFR panel shows the grand average amplitude modulation across frequency around alpha peaks of L5 in V1 ($n = 15$ sessions). White contours indicate significant modulation (random permutation test). Thin horizontal lines mark 90 Hz. *E–H*: same as *A–D* but for area SEF ($n = 16$). All TFRs are scaled to the maximum power modulation in SEF to facilitate interarea comparison. *Insets* below *C* and *G* show the average broadband bipolar LFP of the reference electrode channel (gray area = SE). *I*: laminar distributions of alpha-coupled gamma amplitude for 30–90 Hz (blue) and >90 Hz (red). Asterisks indicate statistical significance (ANOVA with area and frequency as factors using post hoc comparisons, $P < 0.01$ Bonferroni corrected). *J*: alpha phase-dependent distributions of gamma power. Blue dots mark the phase-dependent fraction of amplitude maxima in the 30–90 Hz range, and red denotes the frequency of gamma peaks >90 Hz. Asterisks indicate statistical significance (Rayleigh's test for nonuniformity, $P < 0.01$, Bonferroni corrected). Note the consistent relationship between alpha phase and gamma peaks in V1 compared with the inconsistent patterns in SEF.

ment of V1 and SEF divided into high (>90 Hz) and low (30–90 Hz) gamma frequency bands, respectively. Alpha-coupled gamma amplitudes differed significantly between corresponding laminar compartments of V1 and SEF (ANOVA, $P < 0.01$ followed by post hoc *t*-test, Bonferroni corrected $P < 0.01$; $n = 15$ for V1, $n = 16$ for SEF). Furthermore, in L3 of SEF, alpha-coupled gamma amplitude in the high gamma range was significantly larger than that in the low gamma range.

Phase-amplitude coupling in V1 and SEF also differed in the phase relation between alpha and gamma. The distribution of L5 alpha phase at the maximum gamma amplitude within low- and high-frequency gamma bands revealed different patterns across layers in V1 and SEF (Fig. 5*J*). In V1, the modulatory alpha phase in all layers was significantly different from a uniform distribution (Rayleigh's test for nonuniformity with Bonferroni correction, $P < 0.01$). In contrast, in SEF only in L3 and L5 were the phase distributions significantly different from a uniform distribution (Rayleigh's test for nonuniformity with Bonferroni correction, $P < 0.01$).

The differences between V1 and SEF for gamma coupling with L5 alpha led us to examine whether alpha in other cortical layers would reveal a similar pattern of coupling (Fig. 6). To address this, we measured translaminar gamma coupling to alpha in the middle layers of V1 (L4) and SEF (L3). While the strongest coupling in V1 occurred between alpha in L5 and gamma in L2/3, the strongest coupling in SEF occurred between alpha and gamma within L3 (Fig. 6*A*). In V1, L4 alpha phase also coupled with L2/3 amplitude. Within SEF, L3 showed the greatest power modulation and consistency of coupling. In this layer, coupling of high gamma to alpha was significantly greater than coupling of low gamma to alpha (Fig. 6*B*). Only weak coupling was observed between L2 alpha phase and L3 gamma amplitude.

We next performed a quantitative analysis to evaluate these qualitative differences. We found that the distribution of alpha phase triggered to maximum gamma amplitudes in the middle layers of both V1 and SEF confirmed the results described above. In V1, the distribution of L4 alpha phases was significantly different from uniform for low gamma amplitudes in L5 and low and high gamma amplitudes in L2/3 (Fig. 6*B*) (Rayleigh's test for nonuniformity, $P < 0.01$, Bonferroni corrected). In SEF, the distribution of L3 alpha phases was significantly different from uniform only for high gamma amplitudes in L3 and L5. No significant difference was found for L6 alpha phase in either area.

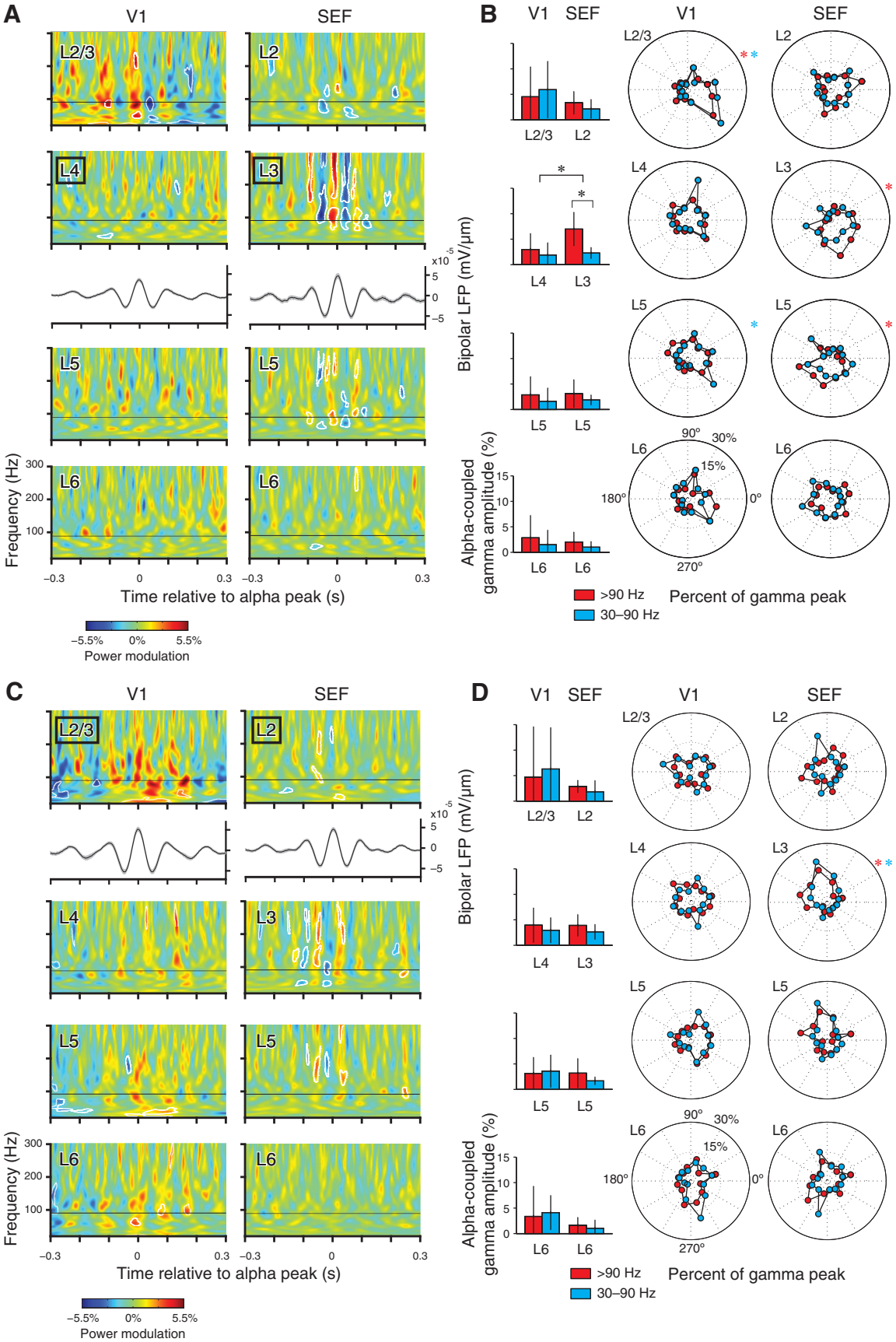
A
V1
SEF
L2/3
L2
L4
L3
L5
L6
x10^-5
5
0
−5
Frequency (Hz)
300
200
100
−0.3
0
0.3
Time relative to alpha peak (s)
−5.5%
0%
5.5%
Power modulation
B
V1
SEF
Bipolar LFP (mV/μm)
Alpha-coupled gamma amplitude (%)
15
10
5
0
90°
30%
15%
180°
0°
270°
>90 Hz
30–90 Hz
Percent of gamma peak
C
D

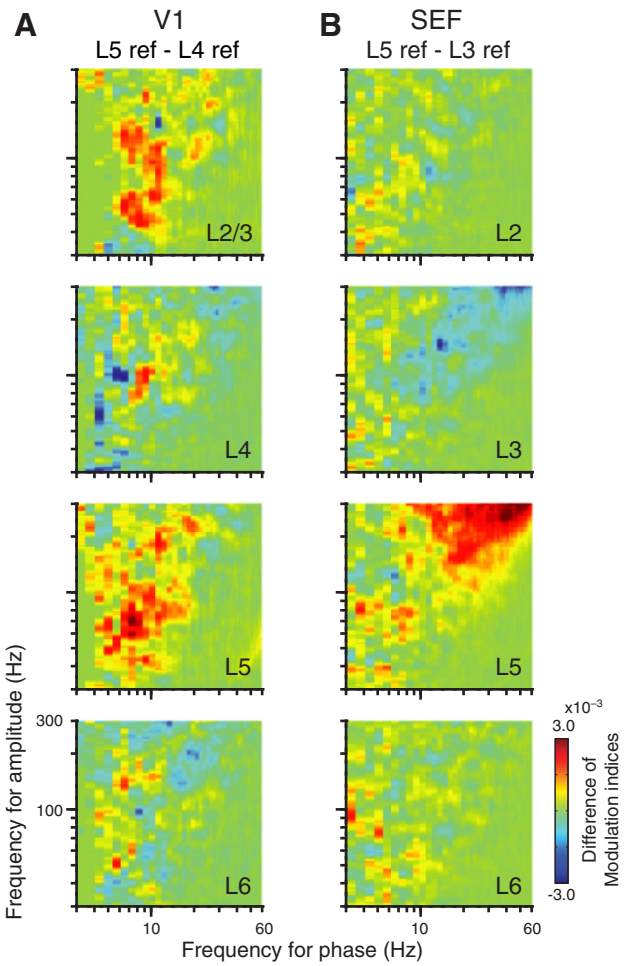

Fig. 7. Difference of interlaminar phase-amplitude coupling as a function of frequency for phase references in different layers of V1 and SEF. Each matrix was obtained by subtracting the Tort MI using L4 (V1) or L3 (SEF) phase-locked signals from L5 phase-locked signals between low-frequency phase (3–60 Hz) and high-frequency amplitude (30–300 Hz) in 1-Hz steps. *A*: frequency-dependent MI across laminar compartments for L4 phase-locked signals subtracted from the MI derived from L5 phase-locked signals in area V1 ($n = 15$). Positive MI values for L2/3 and L5 suggest that gamma amplitude in these layers was coupled stronger with alpha phase in L5 than that in L4. *B*: same as *A* but for a contrast between L3 and L5 phase-locked signals in area SEF. MI patterns for SEF suggest that phase-amplitude coupling was stronger within layers than between L5 and L4 and that these effects were strongest outside of the alpha range. Note the difference in spectral patterns of coupling across layers between V1 and SEF.

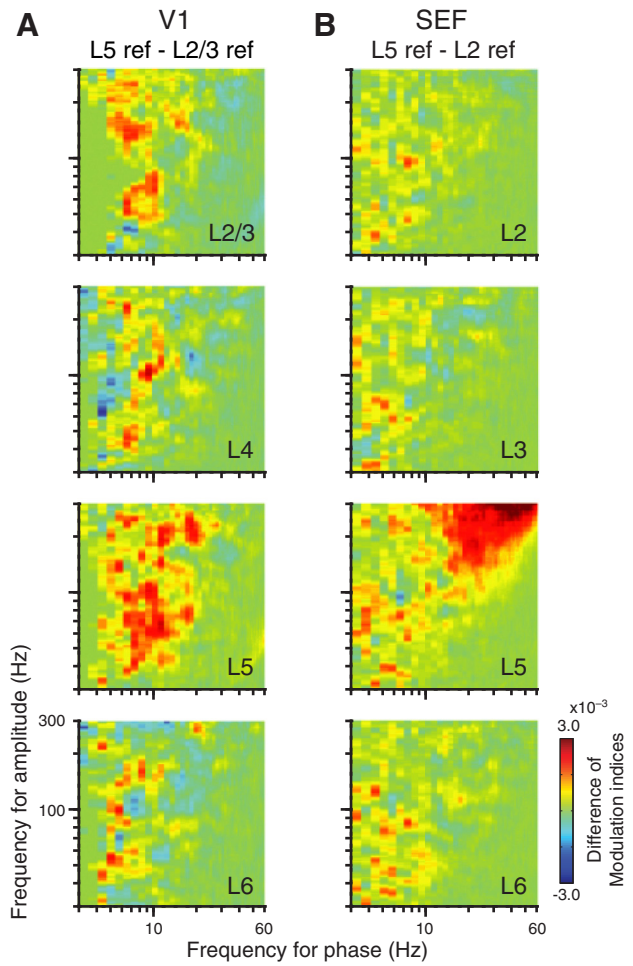

Fig. 8. Difference of interlaminar phase-amplitude coupling between phase references in superficial layers (L2/3 for V1 and L2 for SEF) and L5. All conventions and statistical parameters are identical to those in Fig. 7. *A*: frequency-dependent MI across laminar compartments for L2/3 phase-locked signals subtracted from that derived from L5 phase-locked signals in V1. *B*: same as *A* but for a contrast between L2 and L5 phase-locked signals in SEF.

We also found that the temporal relation between alpha amplitude peaks and maxima of gamma power differed between areas. In V1, the peak of gamma modulation in L2/3 and L5 coincided with the L5 alpha-band peak (Fig. 5, *A*, *C*, *J*; note that the alpha peak corresponds to 0° in the polar plots). Likewise, in SEF the maximum of gamma modulation in L3 coincided with the L5 alpha-band peak (Fig. 5, *F* and *J*). However, in SEF, the maximum of gamma power within L3 preceded the L3 alpha peak (Fig. 6, *A* and *B*). While coupling was weak between L2 alpha LFP and gamma power in L3 and L4 in SEF, the maxima of gamma power occurred on either side of the alpha peak, with reduced power coinciding with the alpha peak (Fig. 6, *C* and *D*).

We tested statistically whether the temporal phase relation between alpha amplitude peaks and maxima of gamma power was different between areas. To accomplish this, we used a permutation test based on Watson's U^2 statistic to compare all cortical layers with phase distributions that were significantly nonuniform ($n = 1{,}000$; $P < 0.01$, Bonferroni corrected). For the high frequency range, we found significant differences between SEF and V1 for L3/L3, L3/L5, and L2/L3 alpha-gamma coupling. In the low gamma range, V1 and SEF differed significantly for L2/L3 coupling. Thus translaminar coupling differs between the low and high gamma range both within and between cortical areas.

Next we asked whether the nonuniform phase relation differed by the layer of alpha reference in V1 and SEF (permu-

Fig. 6. Gamma amplitude coupling to alpha phase from superficial layers of V1 and SEF. Conventions as in Fig. 5. *A* and *B*: TFRs and statistical comparisons for translaminar gamma coupling to alpha phase in L4 (V1, *left*) and L3 (SEF, *right*). *C* and *D*: same as *A* and *B* but for alpha phase from L2/3. V1 data show only minimal gamma modulation with alpha phase in superficial layers. In contrast, SEF gamma power was coupled to the local alpha phase within each respective laminar compartment. Note the phase difference in SEF's alpha-coupled gamma modulation compared with Fig. 5.

tation test based on Watson's U^2 statistic; $n = 1{,}000$; all $P < 0.01$, Bonferroni corrected). We found that in V1 only the temporal phase relation between L4 alpha peaks and L5 gamma power was significantly different from the other phase relations. In contrast, in SEF, the phase relation between L5 alpha peaks and L3 as well as L5 gamma power was significantly different from all other temporal phase relations, suggesting that the temporal structure of phase-amplitude coupling is variable across layers in SEF, in contrast to V1.

Broadband phase-amplitude coupling differences. To determine whether the observed laminar differences between V1 and SEF in phase-amplitude coupling generalize beyond the alpha band, we calculated the MI proposed by Tort et al. (2010). This method results in a single value measuring the degree of coupling between a pair of frequencies for phase and amplitude. The MI was obtained for every combination of frequencies for phase (3–60 Hz) and amplitude (30–300 Hz) and between every combination of pairs of representative channels shown in Fig. 5 and Fig. 6. To facilitate comparison of results using phase references from different laminar compartments, we subtracted the MI maps obtained for each laminar phase reference from a baseline MI map with a L5 phase reference (Fig. 7 and Fig. 8). Note that MI maps based on a L6 phase reference were dropped from further investigation, as statistically significant coupling between phase in this layer and amplitude in the layers above was not observed in either area (see *Phase-amplitude coupling differences*).

In V1, positive MI values were observed between alpha-range (7–14 Hz) phase and gamma amplitudes across all layers, with the most pronounced modulation in L2/3 and L5 (Fig. 7*A* and Fig. 8*A*). Since these plots show the difference in MI for references in L2/3 and L4 compared with L5, the consistency of this pattern suggests that gamma coupling was strongest for alpha in L5 compared with alpha from other layers. This was not the case for SEF. Here again, we found that translaminar coupling was diminished overall, with the strongest effects being outside the alpha range (Fig. 7*B* and Fig. 8*B*). As a whole, the MI analysis confirmed that phase-amplitude coupling is both qualitatively and quantitatively different between V1 and SEF, even outside the frequency bands that we have focused on so far.

Laminar phase-amplitude coupling differences. To concisely summarize the laminar pattern of coupling between the alpha and gamma bands of the LFP in V1 and SEF, the MI values between 7 and 14 Hz (for phase) and between 30 and 200 Hz (for amplitude) were averaged across every electrode combination and across cortical depth. This yielded an MI map with the cortical depth of alpha phase on the *x*-axis and that of gamma amplitude on the *y*-axis (Fig. 9). These interlaminar MI maps confirmed that in V1 the gamma amplitude recorded in L2/3 and in L5 coupled with alpha phase in L5. This interlaminar coupling was absent in SEF. Instead, SEF gamma amplitude in L3 was coupled only to alpha in L3; weaker intralaminar coupling was also observed in L5.

Alpha-aligned current source density differences. We next identified the local origins of the extracellular currents associated with the alpha phase involved in the phase-amplitude coupling above. After detection of alpha peaks in unipolar LFPs in L2/3, L4, L5, and L6 of V1 and in L2, L3, L5, and L6 of SEF, the time-locked laminar CSD was calculated.

In V1, an alternating sink-source pattern straddled the L4/L5 boundary around the time of L5/L6 alpha peaks (Fig. 10*A*). A sink-source pair was also seen in L2/3, where the alpha-coupled gamma power modulation was most pronounced, as described above. These supragranular (L2/3) sink-source pairs were present for alpha references in all cortical layers. The alpha-aligned CSD pattern in SEF was qualitatively different from that for V1, with all sinks and sources restricted to the

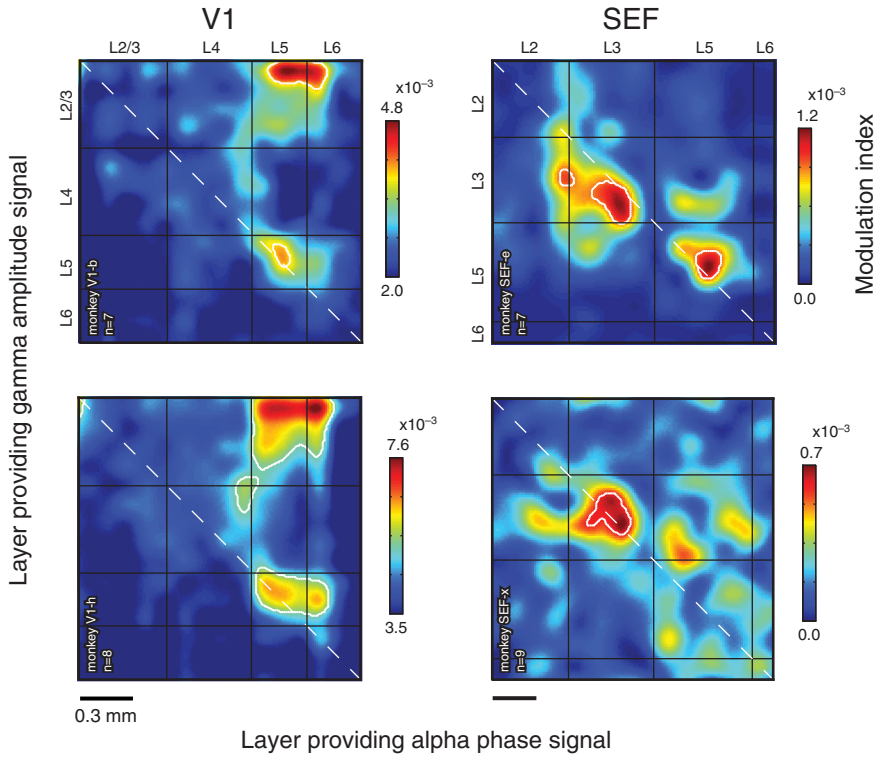

Fig. 9. Laminar organization of phase-amplitude coupling in V1 and SEF shown for individual subjects. Matrices show Tort's MI averaged across cortical depth for alpha phase (*x*-axis) and gamma amplitude (*y*-axis). Borders of L2/3, L4, L5, and L6 in V1 and of L2, L3, L5, and L6 in SEF indicated by black lines. Number of averaged sessions is indicated at *bottom left* of each plot. Significant coupling is indicated by white contours (FDR-corrected $P < 0.01$). Note the similarities across monkeys within each area.

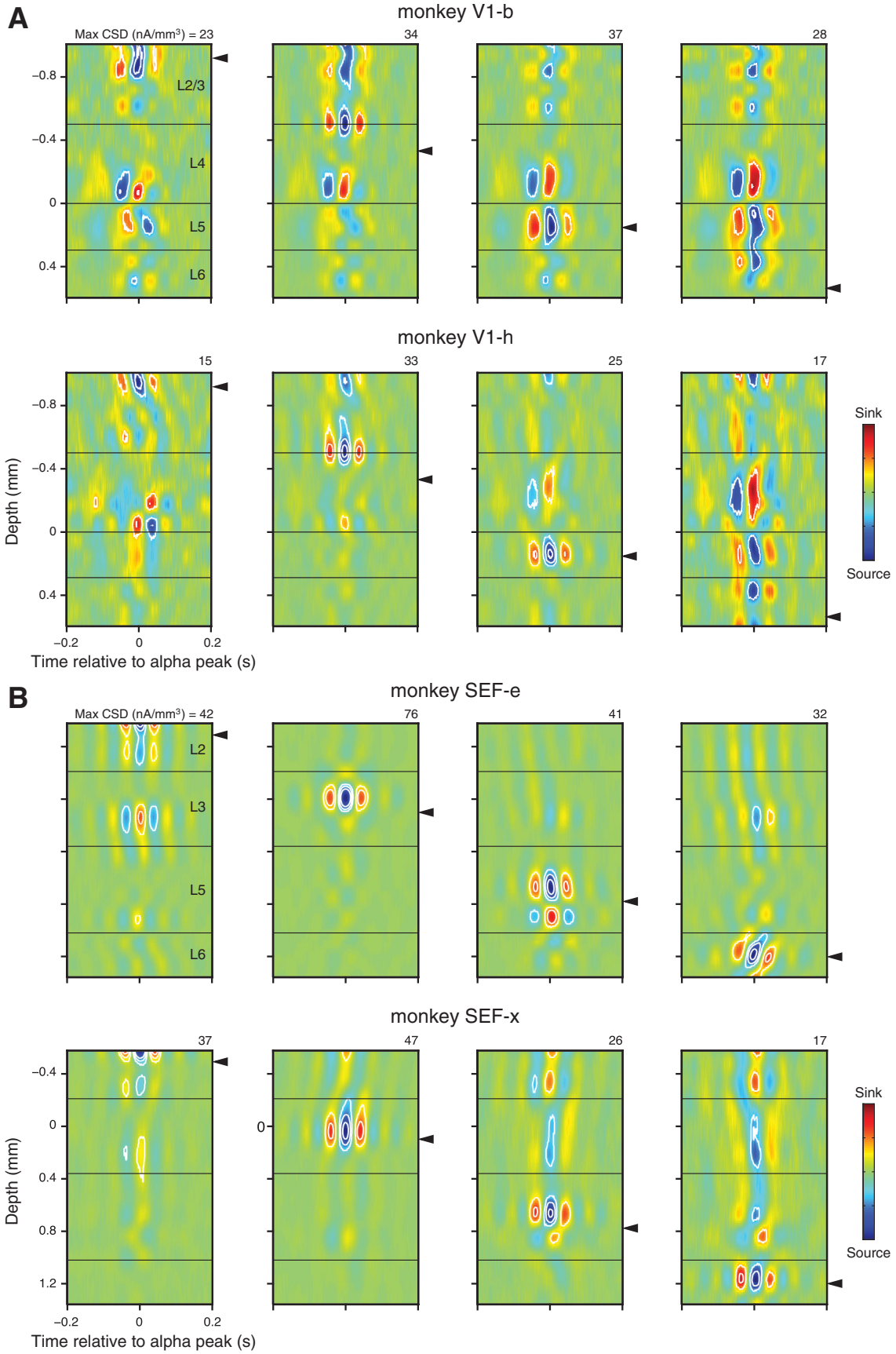
A
monkey V1-b
Max CSD (nA/mm³) = 23
34
37
28
L2/3
L4
L5
L6
monkey V1-h
15
33
25
17
Depth (mm)
Sink
Source
Time relative to alpha peak (s)
B
monkey SEF-e
Max CSD (nA/mm³) = 42
76
41
32
L2
L3
L5
L6
monkey SEF-x
37
47
26
17
Depth (mm)
Sink
Source
Time relative to alpha peak (s)

layer of the alpha reference channel (Fig. 10*B*). Note that the sink-source patterns in the alpha-aligned CSDs were largely consistent across animals in both V1 and SEF. For each area, the alpha-aligned CSD paralleled the distinct patterns of interlaminar and intralaminar coupling within V1 and SEF, respectively.

DISCUSSION

We investigated interlaminar phase-amplitude coupling in granular occipital area V1 and agranular frontal area SEF. We demonstrated, for the first time, phase-amplitude coupling in SEF and replicated a previous report of translaminar coupling in V1 (Spaak et al. 2012). Direct comparison between V1 and SEF revealed pronounced differences across areas. Specifically, we found that V1 and SEF differ in their laminar pattern of coupling, the relative strength of this translaminar coupling, the spectral width of frequencies that are coupled with alpha phase, as well as the temporal phase relation of the cross-frequency coupling.

In V1, prominent interlaminar coupling was observed between the alpha phase in L5 and both low and high gamma power (30–200 Hz) in L2/3 and L5. In SEF, the strongest coupling was observed between alpha phase and high gamma power (90–200 Hz) within L3. Unlike V1, consistent interlaminar interactions were nearly absent in SEF. Congruent with the reduced magnitude and the locally restricted laminar pattern of cross-frequency coupling in SEF, the alpha-aligned CSD profiles in SEF revealed weaker and more restricted current sources than those in V1. These results suggest that the laminar circuitry producing this coupling is quantitatively and qualitatively different between granular V1 and agranular SEF.

Deeper insight on specifics of these regional differences in the organization of local laminar circuits can be gained from CSD analysis. CSD analysis relies on several crucial assumptions about both cortical geometry and electrode parameters that are often difficult to control (Nelson et al. 2008; Tenke et al. 1993). However, none of these theoretical considerations and concerns has proven limiting in practice (Kajikawa and Schroeder 2015). Accordingly, CSD analysis has proven effective as a revealing assay of interlaminar connectivity (Bollimunta et al. 2008, 2011; Spaak et al. 2012). Based on the CSD of the LFP around the time of L5 alpha peaks, Bollimunta and coworkers (2011) reported that alpha generators can be found in all layers of V1. Confirming these results, we found multiple current sinks and sources across the layers of V1 that emerge during alpha peaks in L5. A similar pattern of alpha-aligned CSD was reported for areas V2 and V4 (Bollimunta et al. 2008). These functional similarities among early visual areas are consistent with the hypothesis of a "canonical microcircuit," stating that interlaminar connectivity is preserved across neocortical areas (Callaway 1998; Douglas and Martin 2004; Gilbert 1983). However, the laminar pattern of alpha-aligned CSD in SEF deviated significantly from this general scheme. These functional differences are difficult to explain without allowing for anatomical differences between the cortical microcircuits of V1 and SEF.

It seems conceivable that agranular cortex is a special case among cortical areas–and thus the only exception to the rule. In other words, apart from agranular areas the vast majority of cortex may follow a stereotypical columnar microcircuit with a prominent role for granular L4. Since SEF is thought to lack this central layer, its functional design may be altered to accommodate for this anatomical difference. However, it is worth noting that the spatial extent of granular L4 varies gradually across cortex in the rostro-caudal direction, and whether or not classically defined "agranular" areas are entirely void of L4 is still debated (García-Cabezas and Barbas 2014). The extent to which the laminar pattern of alpha generators and of phase-amplitude coupling found in primary visual cortex generalizes to other cortical areas remains an outstanding question.

As discussed by Spaak et al. (2012), the phase-amplitude coupling of V1 might be explained by the known anatomical microcircuitry of visual cortex. Specifically, the alpha-aligned sink-source patterns straddling the L4/L5 boundary can arise from synchronized synaptic input to the proximal segment of apical dendrites of L5/L6 pyramidal neurons. This localized pattern of activation can spread to interneurons within the same layer (Kapfer et al. 2007; Silberberg and Markram 2007), which project to the superficial layers and modulate activity there (Dantzker and Callaway 2000; Iurilli et al. 2012; Xu and Callaway 2009). Similarly detailed anatomical knowledge about SEF's laminar microcircuit remains lacking, but our results suggest that interlaminar connections in SEF are generally not as prevalent as in V1. It is tempting to speculate that SEF's columnar microcircuit might rely less on interlaminar connectivity because SEF tends to receive input and send output within the same layer. For example, L3 receives input from the mediodorsal nucleus of the thalamus (Erickson and Lewis 2004; Giguere and Goldman-Rakic 1988) and several cortical areas including lateral intraparietal area (LIP), area 7a, and the frontal eye field (FEF) (Barbas and Pandya 1987; Huerta and Kaas 1990; Shipp et al. 1998). At the same time, SEF L3 sends projections to connected areas such as the FEF (Barbas and Mesulam 1981; Huerta et al. 1987). This balanced organization between thalamo-cortical inputs and outputs in SEF is markedly different from the anatomical design of V1, where dense thalamic afferents in the middle layers are spatially segregated from interareal connections above and below (Markov et al. 2014; Sincich and Horton 2005).

Several studies suggest that alpha-band LFPs are generated by neural interactions between the thalamus and the cortex (e.g., Andersen and Andersson 1968; Saalmann et al. 2012; Steriade et al. 1990). In this context, it is interesting to note that the magnitude of coupling and the alpha-aligned current per unit volume were highest in L3 of SEF, where projections from thalamic nuclei, such as the mediodorsal nucleus, preferentially terminate (Erickson and Lewis 2004; Giguere and Goldman-

Fig. 10. Alpha-aligned current source density. *A*: grand average laminar CSD aligned on alpha peak in V1 (*monkey V1-b*, $n = 7$ sessions; *monkey V1-h*, $n = 8$). Alpha reference in L2/3, L4, L5, or L6 from *left* to *right* (marked with arrowhead). Black lines indicate estimated laminar borders. Maximum current per unit volume is indicated at *top right* of each plot. White contours indicate statistically significant difference from zero (FDR-corrected $P < 0.05$). *B*: grand average laminar alpha-aligned CSD in SEF (SEF-e, $n = 7$; SEF-x, $n = 9$). All image conventions as in *A*. Note that interlaminar sink-source pairings were observed in V1 but not in SEF.

Rakic 1988). One possible interpretation of these findings is that SEF L3 might act as a functional equivalent to both granular and extragranular layers of V1. The translaminar coupling between L5 and L2/3 in V1 might be linked to the integration of intra- and interareal information associated with these areas. However, in SEF this process might be restricted to L3, where the main thalamic input meets cortico-cortical connections. The spatially restricted phase-amplitude coupling we observed in SEF thus might be a reflection of a similar type of integrative activity as in area V1, albeit with a different spatial scope.

Recent studies have shown that the gamma range of neural oscillations (>30 Hz) comprises several functionally distinct subbands with different response characteristics (Belluscio et al. 2012; Colgin et al. 2009; Ray et al. 2008; Ray and Maunsell 2011). This spectral distinction is likely also relevant to cross-frequency coupling. However, we did not see systematic differences of coupling between low and high gamma bands for our V1 resting-state data. This finding is not necessarily inconsistent with previous work, because distinctions between low gamma and high gamma activity can depend on stimulation conditions (Ray and Maunsell 2011). Having said this, coupling within the low gamma range (<90 Hz) was largely absent in SEF. This lack of low gamma coupling in SEF suggests that gamma subbands in SEF might reflect a functional division different from that in sensory visual cortex.

In summary, the present study revealed that lamina-specific phase-amplitude coupling occurs in agranular SEF as in early visual areas, but both the magnitude and spatial structure of this coupling are substantially different between areas. These results are difficult to reconcile with the hypothesis of a universal *bauplan* of canonical cortical circuits in all cortical areas (Douglas and Martin 2011).

ACKNOWLEDGMENTS

We thank M. Cox, K. Fukuda, R. Heitz, O. Jensen, D. Leopold, and P. Middlebrooks for reading the manuscript and providing useful comments. We thank D. Boner, M. Feurtado, M. Schall, S. Siegel, C. Suell, N. Tantawy, R. Williams, and G. Wilson for technical assistance.

GRANTS

This work was supported by the Whitehall Foundation, the Alfred P. Sloan Foundation, and National Institutes of Health Grants R01-MH-55806, P30-EY-08126, and P30-HD-015052 and by Robin and Richard Patton through the E. Bronson Ingram Chair in Neuroscience.

DISCLOSURES

No conflicts of interest, financial or otherwise, are declared by the author(s).

AUTHOR CONTRIBUTIONS

Author contributions: T.N., K.D., D.C.G., J.D.S., and A.M. conception and design of research; T.N. and K.D. analyzed data; T.N., K.D., D.C.G., J.D.S., and A.M. interpreted results of experiments; T.N., K.D., D.C.G., J.D.S., and A.M. prepared figures; T.N. and K.D. drafted manuscript; T.N., K.D., D.C.G., J.D.S., and A.M. edited and revised manuscript; T.N., K.D., D.C.G., J.D.S., and A.M. approved final version of manuscript; K.D. and D.C.G. performed experiments.

REFERENCES

Andersen P, Andersson SA. *Physiological Basis of the Alpha Rhythm*. New York: Appleton-Century-Crofts, 1968.

Asaad WF, Eskandar EN. A flexible software tool for temporally-precise behavioral control in Matlab. *J Neurosci Methods* 174: 245–258, 2008.

Barbas H, Mesulam MM. Organization of afferent input to subdivisions of area 8 in the rhesus monkey. *J Comp Neurol* 200: 407–431, 1981.

Barbas H, Pandya DN. Architecture and frontal cortical connections of the premotor cortex (area 6) in the rhesus monkey. *J Comp Neurol* 256: 211–228, 1987.

Belluscio MA, Mizuseki K, Schmidt R, Kempter R, Buzsáki G. Cross-frequency phase-phase coupling between θ and γ oscillations in the hippocampus. *J Neurosci* 32: 423–435, 2012.

Bollimunta A, Chen Y, Schroeder CE, Ding M. Neuronal mechanisms of cortical alpha oscillations in awake-behaving macaques. *J Neurosci* 28: 9976–9988, 2008.

Bollimunta A, Mo J, Schroeder CE, Ding M. Neuronal mechanisms and attentional modulation of corticothalamic α oscillations. *J Neurosci* 31: 4935–4943, 2011.

Brodmann K. *Vergleichende Lokalisationslehre der Großhirnrinde in ihren Prinzipien dargestellt auf Grund des Zellenbaues*. Leipzig, Germany: Barth, 1909.

Callaway EM. Local circuits in primary visual cortex of the macaque monkey. *Annu Rev Neurosci* 21: 47–74, 1998.

Canolty RT, Edwards E, Dalal SS, Soltani M, Nagarajan SS, Kirsch HE, Berger MS, Barbaro NM, Knight RT. High gamma power is phase-locked to theta oscillations in human neocortex. *Science* 313: 1626–1628, 2006.

Canolty RT, Knight RT. The functional role of cross-frequency coupling. *Trends Cogn Sci* 14: 506–515, 2010.

Colgin LL, Denninger T, Fyhn M, Hafting T, Bonnevie T, Jensen O, Moser MB, Moser EI. Frequency of gamma oscillations routes flow of information in the hippocampus. *Nature* 462: 353–357, 2009.

Dantzker JL, Callaway EM. Laminar sources of synaptic input to cortical inhibitory interneurons and pyramidal neurons. *Nat Neurosci* 3: 701–707, 2000.

Douglas RJ, Martin K. Neuronal circuits of the neocortex. *Annu Rev Neurosci* 27: 419–451, 2004.

Douglas RJ, Martin KA. What's black and white about the grey matter? *Neuroinformatics* 9: 167–179, 2011.

Erickson SL, Lewis D. Cortical connections of the lateral mediodorsal thalamus in cynomolgus monkeys. *J Comp Neurol* 473: 107–127, 2004.

García-Cabezas MÁ, Barbas H. Area 4 has layer IV in adult primates. *Eur J Neurosci* 39: 1824–1834, 2014.

Giguere M, Goldman-Rakic PS. Mediodorsal nucleus: areal, laminar, and tangential distribution of afferents and efferents in the frontal lobe of rhesus monkeys. *J Comp Neurol* 277: 195–213, 1988.

Gilbert CD. Microcircuitry of the visual cortex. *Annu Rev Neurosci* 6: 217–247, 1983.

Givre SJ, Schroeder CE, Arezzo JC. Contribution of extrastriate area V4 to the surface-recorded flash VEP in the awake macaque. *Vision Res* 34: 415–428, 1994.

Godlove DC, Garr AK, Woodman GF, Schall JD. Measurement of the extraocular spike potential during saccade countermanding. *J Neurophysiol* 106: 104–114, 2011.

Godlove DC, Maier A, Woodman GF, Schall JD. Microcircuitry of agranular frontal cortex: testing the generality of the canonical cortical microcircuit. *J Neurosci* 34: 5355–5369, 2014.

Hansen BJ, Chelaru MI, Dragoi V. Correlated variability in laminar cortical circuits. *Neuron* 76: 590–602, 2012.

Huerta MF, Kaas JH. Supplementary eye field as defined by intracortical microstimulation: connections in macaques. *J Comp Neurol* 293: 299–330, 1990.

Huerta MF, Krubitzer LA, Kaas JH. Frontal eye field as defined by intracortical microstimulation in squirrel monkeys, owl monkeys, and macaque monkeys. II. Cortical connections. *J Comp Neurol* 265: 332–361, 1987.

Iurilli G, Ghezzi D, Olcese U, Lassi G, Nazzaro C, Tonini R, Tucci V, Benfenati F, Medini P. Sound-driven synaptic inhibition in primary visual cortex. *Neuron* 73: 814–828, 2012.

Jensen O, Colgin LL. Cross-frequency coupling between neuronal oscillations. *Trends Cogn Sci* 11: 267–269, 2007.

Kajikawa Y, Schroeder CE. How local is the local field potential? *Neuron* 72: 847–858, 2011.

Kajikawa Y, Schroeder CE. Generation of field potentials and modulation of their dynamics through volume integration of cortical activity. *J Neurophysiol* 113: 339–351, 2015.

Kapfer C, Glickfeld LL, Atallah BV, Scanziani M. Supralinear increase of recurrent inhibition during sparse activity in the somatosensory cortex. *Nat Neurosci* 10: 743–753, 2007.

Logothetis NK, Kayser C, Oeltermann A. In vivo measurement of cortical impedance spectrum in monkeys: implications for signal propagation. *Neuron* 55: 809–823, 2007.

Maier A, Adams GK, Aura C, Leopold D. Distinct superficial and deep laminar domains of activity in the visual cortex during rest and stimulation. *Front Syst Neurosci* 4: 1–11, 2010.

Maier A, Aura CJ, Leopold D. Infragranular sources of sustained local field potential responses in macaque primary visual cortex. *J Neurosci* 31: 1971–1980, 2011.

Maier A, Wilke M, Aura C, Zhu C, Ye FQ, Leopold DA. Divergence of fMRI and neural signals in V1 during perceptual suppression in the awake monkey. *Nat Neurosci* 11: 1193–1200, 2008.

Maris E, Oostenveld R. Nonparametric statistical testing of EEG- and MEG-data. *J Neurosci Methods* 164: 177–190, 2007.

Markov NT, Vezoli J, Chameau P, Falchier A, Quilodran R, Huissoud C, Lamy C, Misery P, Giroud P, Ullman S, Barone P, Dehay C, Knoblauch K, Kennedy H. Anatomy of hierarchy: feedforward and feedback pathways in macaque visual cortex. *J Comp Neurol* 522: 225–259, 2014.

Matelli M, Luppino G, Rizzolatti G. Architecture of superior and mesial area 6 and the adjacent cingulate cortex in the macaque monkey. *J Comp Neurol* 311: 445–462, 1991.

Mitzdorf U, Singer W. Excitatory synaptic ensemble properties in the visual cortex of the macaque monkey: a current source density analysis of electrically evoked potentials. *J Comp Neurol* 187: 71–83, 1979.

Nelson MJ, Pouget P, Nilsen E, Patten CD, Schall JD. Review of signal distortion through metal microelectrode recording circuits and filters. *J Neurosci Methods* 169: 141–157, 2008.

Nicholson C, Freeman JA. Theory of current source-density analysis and determination of conductivity tensor for anuran cerebellum. *J Neurophysiol* 38: 356–368, 1975.

Oostenveld R, Fries P, Maris E, Schoffelen JM. FieldTrip: open source software for advanced analysis of MEG, EEG, and invasive electrophysiological data. *Comput Intell Neurosci* 2011: 156869, 2011.

Ray S, Crone NE, Niebur E, Franaszczuk PJ, Hsiao SS. Neural correlates of high-gamma oscillations (60–200 Hz) in macaque local field potentials and their potential implications in electrocorticography. *J Neurosci* 28: 11526–11536, 2008.

Ray S, Maunsell JH. Different origins of gamma rhythm and high-gamma activity in macaque visual cortex. *PLoS Biol* 9: e1000610, 2011.

Saalmann YB, Pinsk M, Wang L, Li X, Kastner S. The pulvinar regulates information transmission between cortical areas based on attention demands. *Science* 337: 753–756, 2012.

Schroeder CE, Mehta AD, Givre SJ. A spatiotemporal profile of visual system activation revealed by current source density analysis in the awake macaque. *Cereb Cortex* 8: 575–592, 1998.

Schroeder CE, Tenke CE, Givre SJ, Arezzo JC, Vaughan HG. Striate cortical contribution to the surface-recorded pattern-reversal VEP in the alert monkey. *Vision Res* 31: 1143–1157, 1991.

Self MW, van Kerkoerle T, Supèr H, Roelfsema PR. Distinct roles of the cortical layers of area V1 in figure-ground segregation. *Curr Biol* 23: 2121–2129, 2013.

Shipp S. The importance of being agranular: a comparative account of visual and motor cortex. *Philos Trans R Soc Lond B Biol Sci* 360: 797–814, 2005.

Shipp S, Blanton M, Zeki S. A visuo-somatomotor pathway through superior parietal cortex in the macaque monkey: cortical connections of areas V6 and V6A. *Eur J Neurosci* 10: 3171–3193, 1998.

Silberberg G, Markram H. Disynaptic inhibition between neocortical pyramidal cells mediated by Martinotti cells. *Neuron* 53: 735–746, 2007.

Sincich LC, Horton JC. The circuitry of V1 and V2: integration of color, form, and motion. *Annu Rev Neurosci* 28: 303–326, 2005.

Smith MA, Jia X, Zandvakili A, Kohn A. Laminar dependence of neuronal correlations in visual cortex. *J Neurophysiol* 109: 940–947, 2013.

Spaak E, Bonnefond M, Maier A, Leopold D, Jensen O. Layer-specific entrainment of gamma-band neural activity by the alpha rhythm in monkey visual cortex. *Curr Biol* 22: 2313–2318, 2012.

Steriade M, Gloor P, Llinás RR, Lopes de Silva FH, Mesulam MM. Basic mechanisms of cerebral rhythmic activities. *Electroencephalogr Clin Neurophysiol* 76: 481–508, 1990.

Tenke CE, Schroeder CE, Arezzo JC, Vaughan HG. Interpretation of high-resolution current source density profiles: a simulation of sublaminar contributions to the visual evoked potential. *Exp Brain Res* 94: 183–192, 1993.

Tort AB, Komorowski R, Eichenbaum H, Kopell N. Measuring phase-amplitude coupling between neuronal oscillations of different frequencies. *J Neurophysiol* 104: 1195–1210, 2010.

Walker AE. A cytoarchitectural study of the prefrontal area of the macaque monkey. *J Comp Neurol* 73: 59–86, 1940.

Xing D, Yeh CI, Burns S, Shapley RM. Laminar analysis of visually evoked activity in the primary visual cortex. *Proc Natl Acad Sci USA* 109: 13871–13876, 2012.

Xu X, Callaway EM. Laminar specificity of functional input to distinct types of inhibitory cortical neurons. *J Neurosci* 29: 70–85, 2009.